8-30-2024

Modeling Soil Lateral Deformation Due to Water Film using Smoothed Particle Hydrodynamics

Erly Bahsan
Department of Civil and Environmental Engineering, University of Indonesia, Depok 16424, Indonesia, erlybahsan@eng.ui.ac.id

Budi Susilo Soepandji
Department of Civil and Environmental Engineering, University of Indonesia, Depok 16424, Indonesia, budisus@eng.ui.ac.id

Wiwik Rahayu
Department of Civil and Environmental Engineering, University of Indonesia, Depok 16424, Indonesia, wiwikftui@gmail.com

R.R. Dwinanti R. Marthanty
Department of Civil and Environmental Engineering, University of Indonesia, Depok 16424, Indonesia, dwinanti@gmail.com

Budianto Ontowirjo
Faculty of Engineering, Bakrie University, Jakarta 12940, Indonesia, budianto.ontowirjo@bakrie.ac.id

Follow this and additional works at: https://scholarhub.ui.ac.id/mjt

Part of the Geotechnical Engineering Commons

Modeling Soil Lateral Deformation Due to Water Film using Smoothed Particle Hydrodynamics

Erly Bahsan[1*], Budi Susilo Soepandji[1], Wiwik Rahayu[1],
R.R. Dwinanti R. Marthanty[1], and Budianto Ontowirjo[2]

1. Department of Civil and Environmental Engineering,
University of Indonesia, Depok 16424, Indonesia
2. Faculty of Engineering, Bakrie University, Jakarta 12940, Indonesia

*E-mail: erlybahsan@eng.ui.ac.id

Abstract

In geotechnical engineering, large deformation in soil materials is rarely simulated using numerical methods, particularly the finite element method and finite difference method, because they experience difficulties in representing the postfailure soil behavior. As an alternative to these methods, the smoothed particle hydrodynamics (SPH) method has recently been adopted to represent soil behavior. The SPH method is a Lagrangian, mesh-free numerical method in which the materials are modeled as a set of particles. In this method, soil behavior can be represented via the Drucker–Prager elasto–plastic failure criterion. Thus, this method can be used to simulate postfailure soil behavior and large deformation in soil materials. This study attempts to analyze large deformation of soil due to an extremely gentle slope and a thin water layer (referred to as the water film). The model is simulated using a C++ platform called PersianSPH. The results demonstrate that lateral deformation can occur in such a geometry because of the effective stress changes during liquefaction.

Keywords: large deformation, numerical method, smoothed particle hydrodynamics, soil behavior, water film

1. Introduction

In practical geotechnical engineering, the phenomena of postfailure deformation are seldom studied because of the limitations of the widely known numerical methods such as the finite element method or finite difference method. However, one must study soil conditions after failure, particularly if they are associated with large deformation that could considerably impact the structures on the soil surface the notable phenomena of lateral deformation occurred following the massive earthquake in Central Sulawesi, Indonesia, in 2018. Recently the smoothed particle hydrodynamics (SPH) method has been adopted in several studies in geomechanics. This method is considered more suitable for modeling of large soil deformation.

SPH is a mesh-free particle method based on Lagrangian formulation, and it was first applied to solve astrophysical problems in open space [1–3]. Recently, this method has also been applied for geomaterials and geodisaster models [4–6]. Some examples of applications of SPH in geotechnical cases are for dam-break analysis [7], large deformation and slope failure [8], seepage [9], liquefaction [10], and interaction between fluid flow and solid material

[11]. This study attempts to analyze a model of presumably large deformation of layered soil due to a gentle slope and a thin layer of water (referred to as the water film [12]). Previous studies attempted to develop a Fortran code to represent a soil–water model using SPH [13]. The recent simulation has been conducted using an open-source C++ code platform called PersianSPH [14, 15]. This study expands the new possibility of representing the large deformation and the effect of water film using a numerical method, in comparison with the previous laboratory-based models [16, 17].

2. Basic Concept of SPH

The basic concept of SPH [8, 18–20] is that a state of system is represented by a set of particles, which possess material properties and interact with each other within a range controlled by a smoothing function. SPH is built on the interpolation theory with two essential aspects, kernel approximation and particle approximation. For example, let us consider a particle α surrounded by other particles β, as shown in Figure 1. The value of a function at this main particle α is approximated using the average of the values of the function at all particles in the influence domain of particle α, weighted by the smoothing function

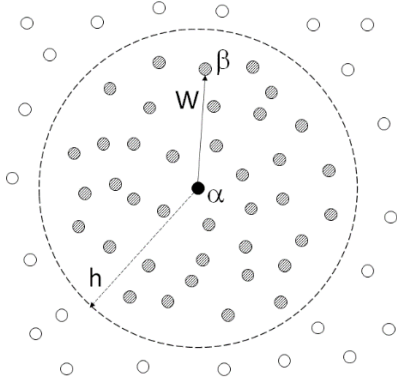W. The neighboring particles β are influenced by α within the range of h.

Figure 1. Typical Particle Arrangement in the Smoother Particle Hydrodynamics (SPH) Method

The kernel approximation can be expressed as a function f(x) as the position of vector x as follows:

$$\langle f(x) \rangle = \int_{\Omega} f(x')W(x-x',h)dx' \qquad (1)$$

The particle approximation can be expressed as follows:

$$\langle f(x) \rangle = \sum_{j=1}^{N} \frac{m_j}{\rho_j} f(x_j)W(x-x_j',h) \qquad (2)$$

This particle approximation is responsible for the mass and density of the SPH particles within the computational domain.

The Navier–Stokes equations is used as the governing equation for representing the motion of the particles. It is formulated as a continuity equation as follows:

$$\frac{D\rho}{Dt} = \sum_{j=1}^{N} m_j v_{ij}^{\beta} \frac{\partial W_{ij}}{\partial x_i^{\beta}} \qquad (3)$$

and the momentum equation is expressed as follows:

$$\frac{Dv_i^{\alpha}}{Dt} = \sum_{j=1}^{N} m_j \left(\frac{\sigma_i^{\alpha\beta}}{\rho_i^2} + \frac{\sigma_j^{\alpha\beta}}{\rho_i^2} \right) \frac{\partial W_{ij}}{\partial x_i^{\beta}} + F_i \qquad (4)$$

The term $\frac{m}{\rho}$ represents the ratio between mass and density, v velocity, α and β directions of coordinate, $\sigma^{\alpha\beta}$ the stress tensor, and F external forces.

The soil model in SPH as adopted from [21] represents the stress tensor via isotropic pressure p and deviatoric shear stress $s^{\alpha\beta}$:

$$\sigma^{\alpha\beta} = -p\delta^{\alpha\beta} + s^{\alpha\beta} \qquad (5)$$

where $\delta^{\alpha\beta}$ represents the Kronecker delta.

The isotropic pressure p is defined as follows:

$$p = -\frac{\sigma^{\gamma\gamma}}{3} = K\epsilon^{\gamma\gamma} \qquad (6)$$

where K represents bulk modulus and $\epsilon^{\gamma\gamma}$ volumetric strain.

The soil's plastic behavior is governed by a soil failure criterion, which is the Drucker–Prager criterion:

$$f(I_1, J_2) = \sqrt{J_2} + \alpha_{\phi} I_1 - k_c = 0 \qquad (7)$$

where I_1 and J_2 represent the first invariant of the stress tensor and the second invariant of the deviatoric stress tensor, respectively:

$$I_1 = \sigma^{xx} + \sigma^{yy} + \sigma^{zz} \quad and \quad J_2 = \frac{1}{2}\dot{s}^{\alpha\beta}\dot{s}^{\alpha\beta} \qquad (8)$$

The Drucker–Prager constants in eq. (7), α_{ϕ} and k_c, are related with the cohesion c and friction angle ϕ as follows:

$$\alpha_{\phi} = \frac{\tan\phi}{\sqrt{9+12\tan^2\phi}} \qquad (9)$$

$$k_c = \frac{3c}{\sqrt{9+12\tan^2\phi}} \qquad (10)$$

3. Geometry Models

Four two-dimensional (2D) soil models with various geometries were built using the platform PersianSPH, as shown in Figures 2–5. These models were simplification of the actual case of the lateral deformation that occurred in Sulawesi Tengah following the strong earthquake in 2018. They aimed to assess several conditions regarding the cause of the lateral deformation, such as the inclined surface, layered soils, and thin water film. The first model (Model 01) comprised two different layers with flat surface, and a ground water level at the surface. It had homogeneous noncohesive soil with a relatively gentle slope of 10% and near-surface water level (Figure 2). It aimed to check the behavior of a saturated, noncohesive soil with sloping surface. The second model (Model 02) comprised a sloping surface (10%) with two different soil layers: cohesive and noncohesive, without water level (Figure 3). The third model (Model 03) had two different soil layers (cohesive and noncohesive) separated by a thin water film (Figure 4). As seen from Figure 5, the last model was the same as the third model but with a gentler slope (5%). The length of the geometry from the left to right boundaries was 25.8 m, and the height of the left- and right-side boundaries were 3.375 and 5.375 m, respectively. The thin water film introduced in Models 03 and 04 was 0.02 m in thickness. These SPH models

were executed through certain time steps to observe the behavior of the models vis-à-vis shape/position, stress, strain, and deformation.

Table 1 presents the typical soil parameters used in this simulation. These parameters were the simplification
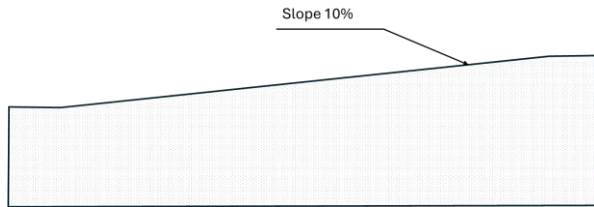
from the actual condition in Sulawesi Tengah following the 2018 earthquake, which consisted of two main layers of soils: cohesive and noncohesive [22–24]. The noncohesive layer was characterized by lower cohesion number and larger soil particle size, while the cohesive layer had higher cohesion and smaller soil particle size.

Figure 2.   Model 01: Homogeneous Noncohesive Model
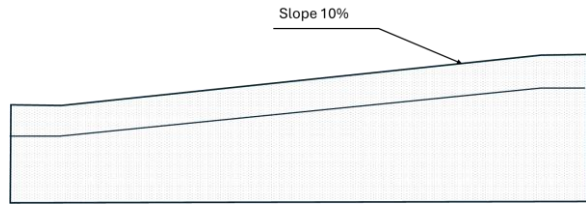
Figure 3.   Model 02: Cohesive Layer Overlays Noncohesive Layer without Water Level
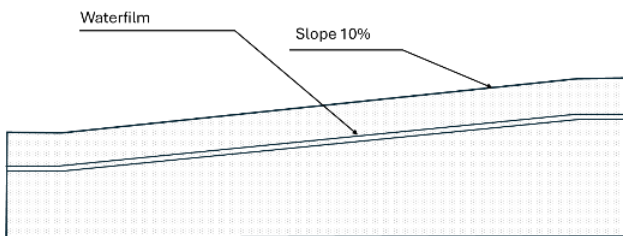
Figure 4.   Model 03: Cohesive Layer Over Noncohesive Layer with Water Film
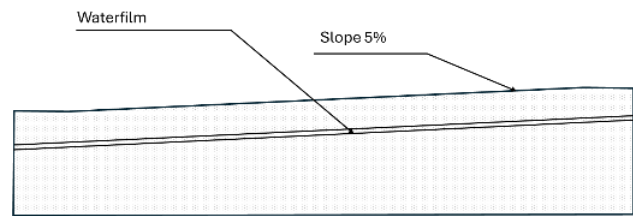
Figure 5.   Model 04: gentler slope

Table 1.   Typical Soil Parameters used in this Study

Parameter	Notasi	Cohesive	Non-cohesive	Units
Density	γ	18	18	(Kn/m^3)
Cohesive	c	10	0.5	(Kn/m^2)
Friction angle	ϕ	20	20	(derajat)
Grain Size	d	0.0002	0.002	(m)
Porosity	n	0.35	0.35	

4. Results and Discussion

In SPH, the position of each particle is calculated for each time step. Here, time step is a unitless time deviator representing a certain step through the simulation. In this study, the simulation was limited to 200 time steps, except for Model 03, to see the end of the particles' movement. Outputs of the simulations were visually plotted in the software Visit.

Visual observation of the models. Changes were observed in geometry of each of the four models; see Figures 6–9.

From Figure 6, one can see that no considerable changes occurred in geometry of the saturated noncohesive deposit with sloping surface as represented by Model 01. Still, the particles were slightly displaced without reaching the failure condition.

Model 02 in Figure 7 is even more stable than Model 02. One can conclude that the lower water level had a dominant effect in stability despite adding the cohesive layer above the noncohesive layer.

Figure 8 shows Model 03 as two different layers, one cohesive and the other noncohesive, with a thin water layer between the two. One can see a change in position of the particles at the top layer and the bottom noncohesive layer. Model 04 (Figure 9), with a gentler slope of 5%, also shows considerable movement of particles. These results confirm the notable effect of the thin water film in causing deformation.

Effective stress condition. The effective stress condition was observed from the visual interpretation in the software Visit. In SPH, the default for effective stress as tension is a sign with negative value, while positive

means tensile stress. "Visit" expressed the effective stress of particle as a tensor visualized by a balloon-like figure with color gradation that represent the values. The shape of the balloon represented the resultant of the stress tensor components. Figure 4 shows visualization of the effective stress tensor at the end of simulation for the first model.

To further check the effective stress profile, the vertical effective stress of the particles were observed along Sections of A and B, as shown in Figure 11.

The effective stress profiles for Model 01 at the beginning and end of simulation are shown in Figure 12 and 13, respectively. In the figures amount of vertical effective stress is represented by orange dots, and analytical

prediction of the effective stress profile is shown by the dashed black line.

Figures 14–20 show the effective stress condition at the end of the simulation for Models 02, 03, and 04.

Figures 12 and 17 show the effective stress profiles for Models 01 and 03 at the beginning of the simulation, respectively. One can see that the effective stress condition at below the water level is less than the theoretical condition. Presumably, at the beginning of the simulation, the pore pressure increases and hence the effective stress decreases. This condition can be interpreted as static liquefaction. At the end of the simulation, the pore pressure decreased and the effective stress restored to the presumed condition.
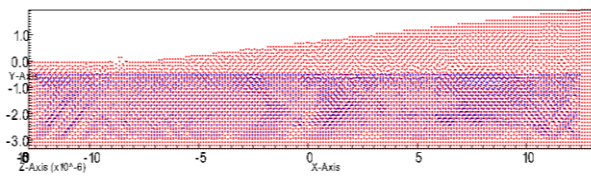
Figure 6. End Result of Model 01
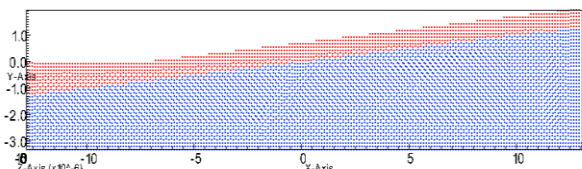
Figure 7. End Result of Model 02
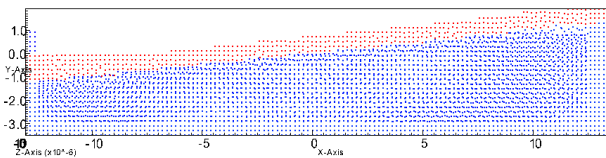
Figure 8. End Result of Model 03
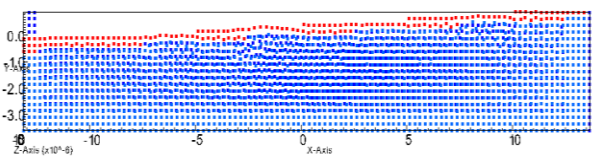
Figure 9. End Result of Model 04
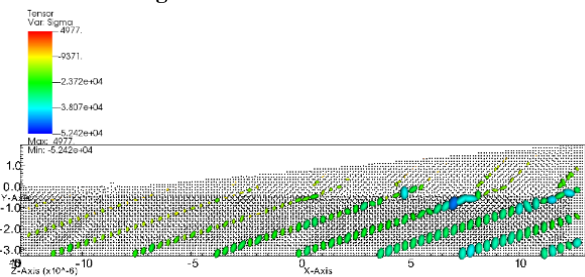
Figure 10. Stress Tensor Condition After Simulation for Model 01
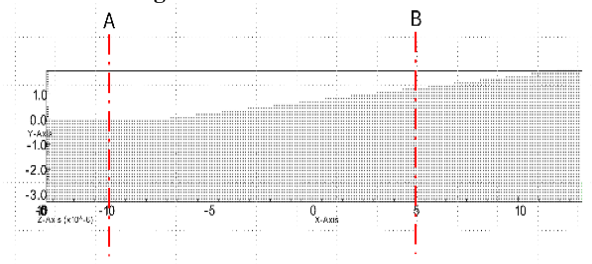

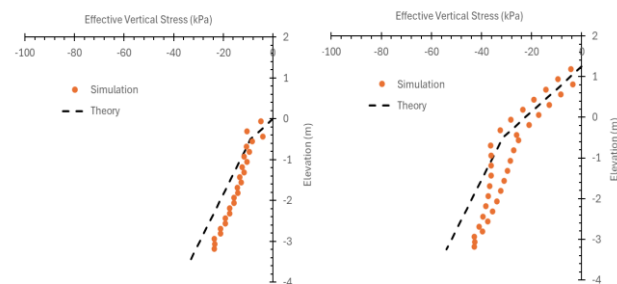**Figure 11. Sections A and B for Observing the Effective Stress Profile**

Figure 12. Effective Stress Profile of Model 01 at the Beginning of the Simulation
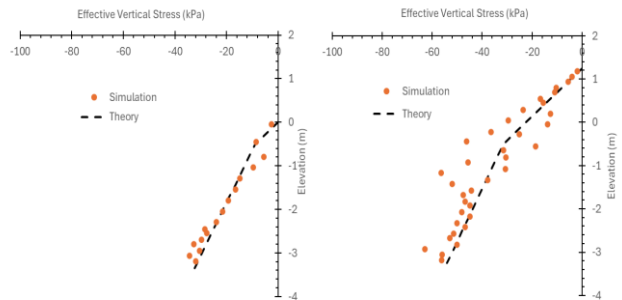

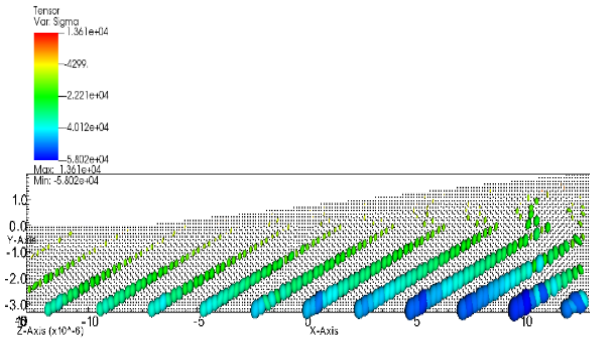**Figure 13. Effective Stress Profile of Model 01 at the End of the Simulation**

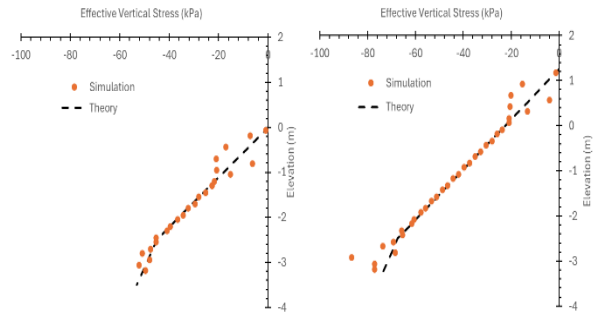**Figure 14. Stress Tensor Condition After Simulation for Model 02**

Figure 15. Effective Stress Profile of Model 02 at the End of the Simulation
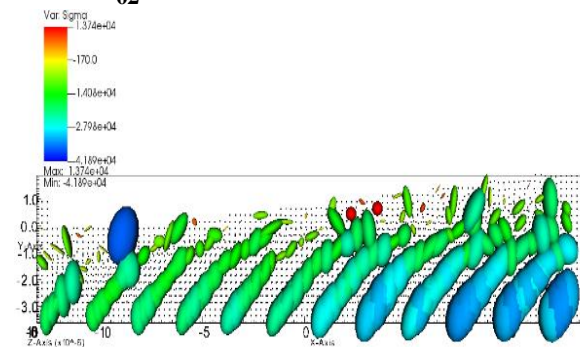

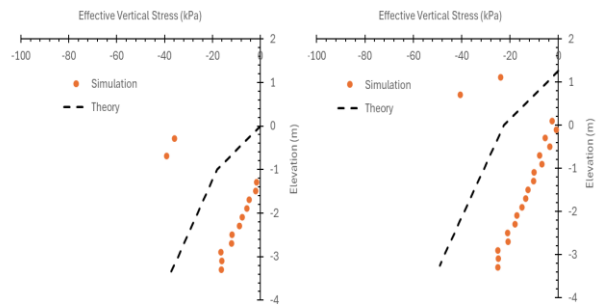**Figure 16. Stress Tensor Condition After Simulation for Model 03**

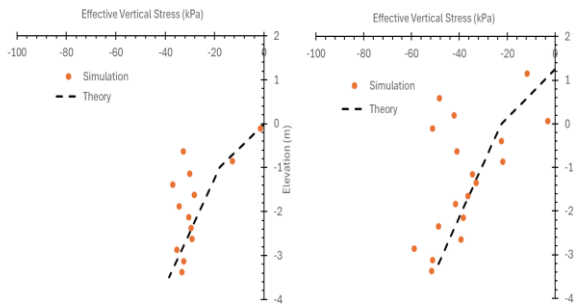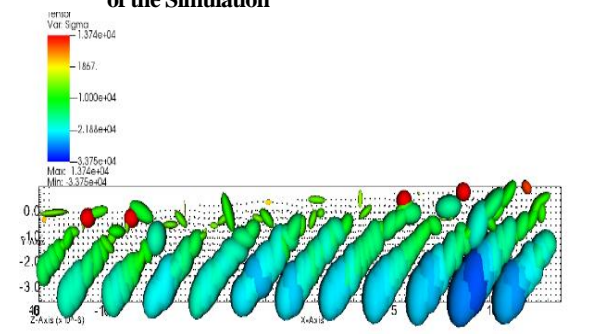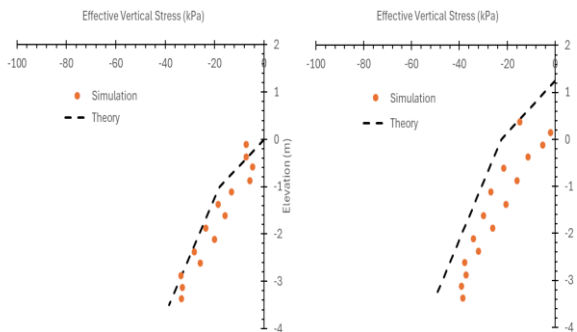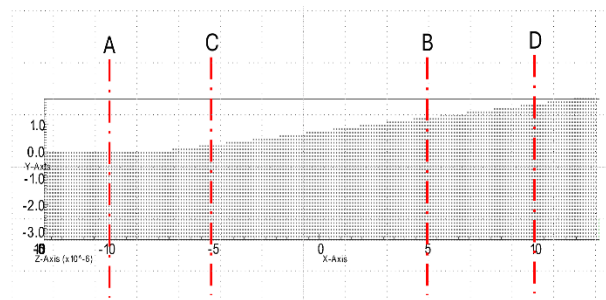**Figure 17. Effective Stress Profile of Model 03 at the Beginning of the Simulation**

Figure 18. Effective Stress Profile of Model 03 at the End of the Simulation

Figure 19. Stress Tensor Condition After Simulation for Model 04

Figure 20. Effective Stress Profile of Model 04 at the End of the Simulation

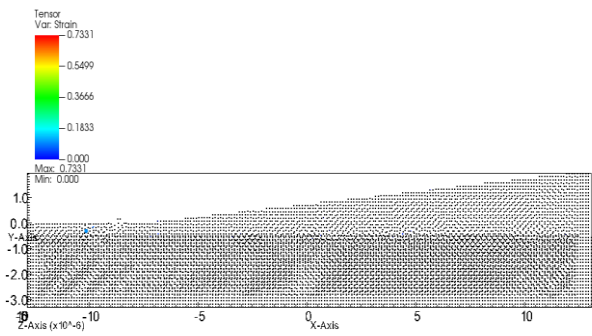**Figure 21. Sections A, C, B, and D for Observing the Effective Stress**

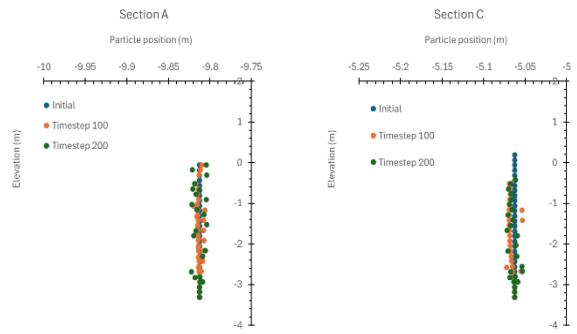**Figure 22.** **Strain Tensor Condition After Simulation for Model 01**

Figure 23. **Particles' Position from the Beginning to the End of Simulation for Model 01 at Sections A and C**
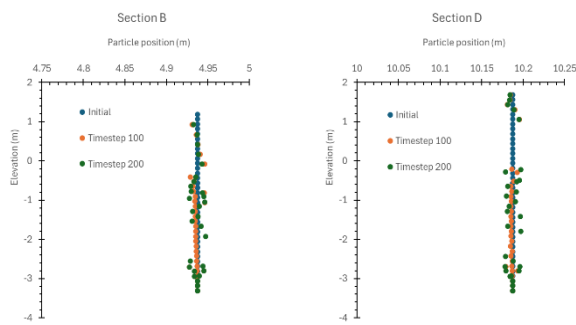

Figure 24. **Particles' Position from the Beginning to the End of Simulation for Model 01 at Sections B and D**
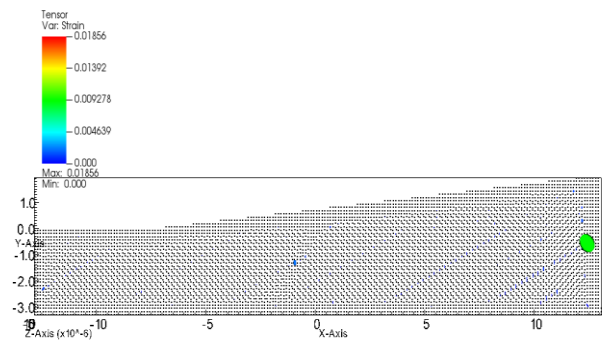

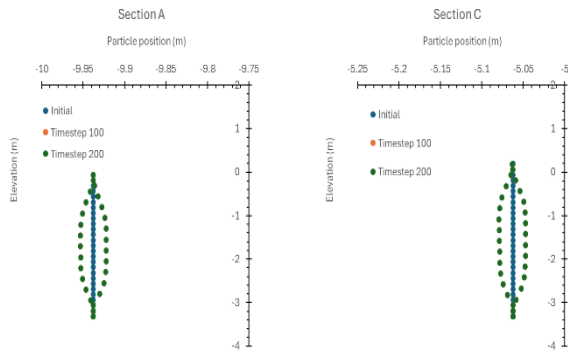**Figure 25.** **Strain Tensor Condition After Simulation for Model 02**

Figure 26. **Particles' position from the beginning to end of Simulation for Model 02 at Sections A and C**

Figure 27. **Particles' position from the beginning to the end of Simulation for Model 02 at Sections B and D**

Figure 28. **Strain Tensor Condition After Simulation for Model 03**

Figure 29. **Particles' Position from the Beginning to End of Simulation for Model 03 at Sections A and C**
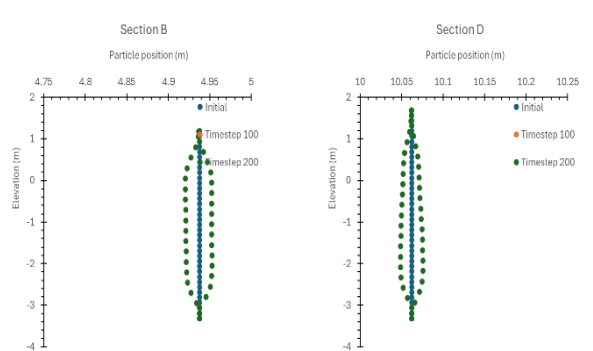
Figure 30. Particles' Position from the Beginning to End of Simulation for Model 03 at Sections B and D
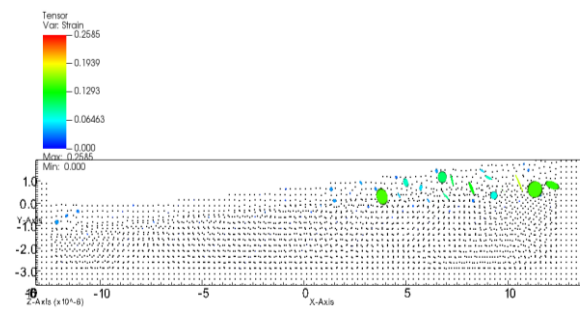

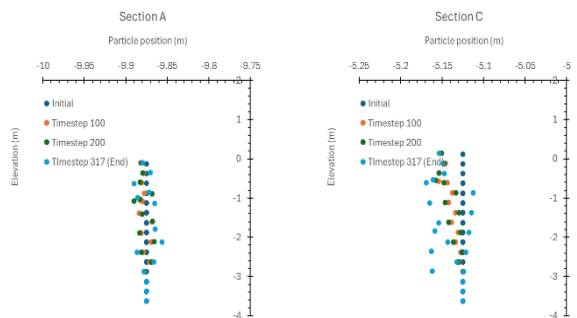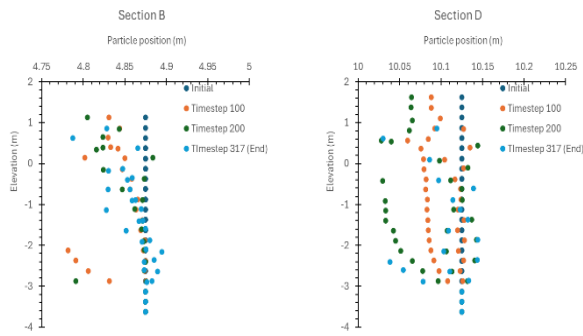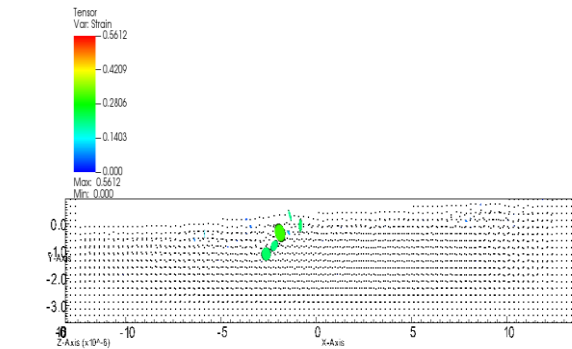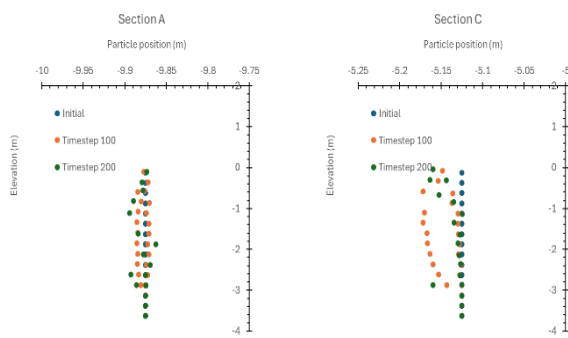**Figure 31. Strain Tensor Condition After Simulation for Model 04**

Figure 32. Particles' Position from the Beginning to End of Simulation for Model 04 at Sections A and C
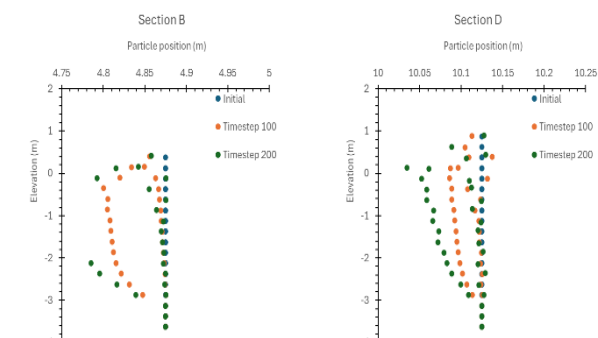

Figure 33. Particles' Position from the Beginning to End of Simulation for Model 04 at Sections B and D
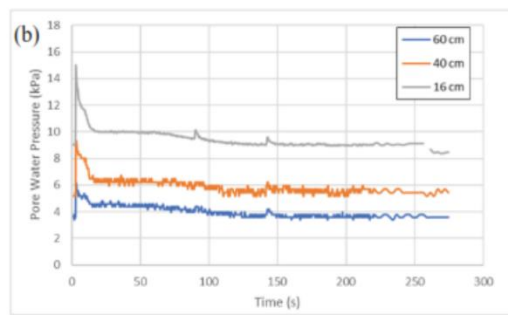

Figure 34. Effective Stress Conditions from the Laboratory Test in [16]

Figures 16 and 19 show the stress tensor condition at the end of simulation for Models 03 and 04, respectively. Clearly, the effective stress at the top layer is extremely small to negative (red color on the tensor balloon) while the effective stress at the bottom layer is higher. One can interpret that the top layer was in the failure condition and highly likely moved, while the bottom layer became denser and more stable. This is similar to the after-liquefaction condition [16, 17].

Strain and deformation after simulation. The strain output from the simulation is visualize as tensor strain as well as the stress, using the balloon-shape figure with color gradation. To observe the exact movement of particles, their positions were tracked before and after the simulation at Sections A, C, B, and D (as addition to the previously introduced Section A and B), as shown in Figure 21.

Figures 22–33 show the strain tensor and the particles' positions at the aforementioned sections both at the beginning and end of the simulation for Models 01, 02, 03, and 04.

From the strain tensor condition and the particles' position, it is confirmed that the largest deformation among the four models occurred for Models 03 and 04 at the end of simulation. One can conclude that the water film between two soil layers is one of the important

factors causing soil lateral deformation irrespective of the shear strength parameters of the soils.

Regarding the effective stress conditions shown in Figures 12–20, the laboratory test results [16] showed that the effective stress below the water film increased at the beginning of the liquefaction and suddenly dropped until the end of liquefaction.

5. Conclusion

Simulation results obtained with PersianSPH showed that lateral deformation occurred in a model with two different soil layers, namely a cohesive layer atop a noncohesive layer, with a thin water layer between the two soil layers. In the 2D model used with a model length of 25.8 m and a surface slope of 10%, deformation was observed in the soil layer above the thin water layer of 7–10 cm. However, this deformation did not occur in models with the same geometry albeit without a thin water layer. This confirms that "thin water layer" and "slope of the surface" are two factors that can induce lateral deformation.

References

[1] G.R. Liu, M.B. Liu, Comput. Mech. 33 (2004) 491.
[2] L.B. Lucy, Astron. J. 82/12 (1977) 1013.
[3] R.A. Gingold, J.J. Monaghan, Mon. Not. R. Astron. Soc. 181/3 (1977) 375.
[4] M.R. Islam, M.A. Rahman, K. Hayano, SN Appl. Sc. 2/4 (2020) 14.
[5] H. Niroumand, M.E.M. Mehrizi, M. Saaly, Geomech. Eng. 11/1 (2016) 39.
[6] Y. Huang, Z. Dai, Eng. Geol. 168 (2014) 86.
[7] Z. Wang, H.T. Shen, J. Hydraul. Eng. 125/11 (1999) 1217.
[8] H. H. Bui, R. Fukagawa, and K. Sako, "Smoothed particle hydrodynamics for soil mechanics," in Numerical Methods in Geotechnical Engineering. London: Taylor & Francis Group, 2006.
[9] K. Maeda, M. Sakai, J. Appl. Mech. 7 (2004) 775.
[10] M. Naili, T. Matsushima, Y. Yamada, J. Appl. Mech. 8 (2005) 591.
[11] R.P. Suntarto, J. Sjah, R.R.D. Rika, E. Bahsan, IOP C. Ser. Earth Env. 1169/1 (2023) 012039.
[12] T. Kokusho, Soil Dyn. Earthq. Eng. 23/7 (2003) 585.
[13] E. Bahsan, B. Andreatama, W.A. Prakoso, B.S. Soepandji, R.R.D.R. Marthanty, Int. J. Technol. 12/5 (2021) 965.
[14] M.G. Korzani, S.A. Galindo-Torres, A. Scheuermann, D.J. Williams, Acta Geotech. 13/2 (2018) 303.
[15] M.G. Korzani, S.A. Galindo-Torres, A. Scheuermann, D.J. Williams, Water Sci. Eng. 10/2 (2017) 143.
[16] M.I. Tanjung, M. Irsyam, A. Sahadewa, S. Iai, T. Tobita, H. Nawir, Proceedings of the 4th International Conference on Performance Based Design in Earthquake Geotechnical Engineering, Beijing, China, 2022, p.565.
[17] T. Kokusho, Soils Found. 40/5 (2000) 99.
[18] M.B. Liu, G.R. Liu, Arch. Comput. Method. E. 17/1 (2010) 25.
[19] H.H. Bui, K. Sako, R. Fukagawa, J.C. Wells, The 12th International Conference of International Association for Computer Methods and Advances in Geomechanics (IACMAG), Goa, India, 2008, p.570.
[20] M.G. Korzani, S.A. Galindo-Torres, D. Williams, A. Scheuermann, Appl. Mech. Mater. 553 (2014) 168.
[21] M.G. Korzani, S.A. Galindo-Torres, A. Scheuermann, D.J. Williams, Comput. Geotech. 94 (2018) 31.
[22] W. Rahayu, Nurizkatilah, E. Bahsan, IOP C. Ser. Earth Env. 622/1 (2021) 012016.
[23] W. Rahayu, I. Yuliyanti, E. Bahsan, IOP C. Ser. Earth Env. 622/1 (2021) 012015.
[24] I.M. Watkinson, R. Hall, Nat. Geosci. 12/11 (2019) 940.
[25] T. Kokusho, J. Geotech. Geoenviron. 125/10 (1999) 817.